Requirements for corrosion inhibitor release from damaged primers for stable protection
A simulation and experimental approach using cerium loaded carriers

Denissen, Paul J.; Homborg, Axel M.; Garcia, Santiago J.

Important note
To cite this publication, please use the final published version (if applicable).
Please check the document version above.

Requirements for corrosion inhibitor release from damaged primers for stable protection: A simulation and experimental approach using cerium loaded carriers

Paul J. Denissen [a], Axel M. Homborg [b], Santiago J. Garcia [a],[*]

[a] *Novel Aerospace Materials group, Faculty of Aerospace Engineering, Delft University of Technology, Kluyverweg 1, 2629 HS Delft, the Netherlands*
[b] *Netherlands Defence Academy, Het Nieuwe Diep 8, 1781 AC Den Helder, the Netherlands*

ABSTRACT

In this work a diffusion-driven inhibitor transport model is used to help in the design of inhibitor-loaded carriers for anticorrosive primers. The work focuses on inhibitor release at damaged locations of different dimensions exposed to electrolyte and is validated experimentally. The damage dimensions are first simulated to determine the minimal inhibitor release rate necessary to reach the required inhibitor concentrations for corrosion protection of the exposed metal. Kinematic and mass conservation laws are then used as first-order approximations to study the effect of different characteristics of nano- and micro-particles loaded with inhibitors embedded in an organic coating during the first 100 s of immersion. The simulated results are validated experimentally using epoxy coatings containing cerium-loaded zeolites and diatomaceous earth as nano- and micro-carriers respectively. These experiments confirmed the simulated predictions, showing that under the used exposure conditions nano-particles are only able to protect relatively small damages of micron size dimensions. Micron-sized carriers on the other hand allow sufficient release to protect larger damages, even at lower pigment volume concentrations. Additional simulations on rapid electrolyte diffusion pathways inside the coating are also in good agreement with the experiments, indicating the presence of diffusion pathways might play an important role in sustained inhibitor release and corrosion protection at local damages.

1. Introduction

Organic coatings have the primary function to protect metal surfaces from aggressive environmental conditions by a well-adhering passive barrier layer [1,2]. This layer stops or significantly hinders the transport of aggressive species, thereby preventing corrosion processes occurring at the metal substrate [3,4]. Nevertheless, environmental factors (e.g. mechanical stresses, thermal cycles and moisture) can cause micro- and macroscopic defects in the coating, resulting in a local loss of protection [5–7].

Corrosion inhibitors are incorporated in the coatings to provide additional protection in case of local through-coating damages or after barrier loss. Under such circumstances the inhibitor leaches from the coating surrounding the damaged site towards the exposed metal and protects it by blocking anodic and/or cathodic active regions. Hence, the ideal coating should reduce the diffusion of aggressive species while, in case of failure, allow a sufficiently fast transport of enough inhibitor

through the coating for active protection [8,9].

Over the past decades a few studies have shown that particle networks and connectivity are important factors for the transport of leachable inhibitors through the coating [10–15]. Tomography techniques showed that inhibitor release in Strontium chromate ($SrCrO_4$) containing primers is dependent on the creation of large clusters of chromate micro-particles via void pathways [10,11]. Other studies involving inhibitor salts have shown the importance of the coating composition and pigment volume concentration (PVC) [12–15] and modelled the effects of inhibitor diffusion through the coating [16–20] and as function of pH [17–20] and damage size [18–20].

Modeling of inhibitor release from the coating walls at through-thickness damage locations is complex when all factors are considered. This is due to the large amount of unknowns such as the rates of electrochemical reactions at the metal surface involving local inhibitor deposition, equilibrium conditions at the metal surface, local swelling and hydrolysis in the coating, the release and transport of inhibiting

species through the various interfaces and finally the heterogeneity of the coating [21,22]. For this reason studies in the field include clearly defined boundary conditions set by a number of assumptions to simplify the problem yet allowing for relevant information to be retrieved. The transport of inhibitors from the coating-damage interface under immersion conditions, sometimes referred to as the chemical throwing power [18], has been described as a diffusion-driven process based on Fick's law [18,23]. On the other hand, several other studies have shown that non-Fickian diffusion models are required to accurately describe the inhibitor transport inside the coating [21,22,24,25]. While these simulations give insight in the release mechanisms, they are rarely used during the development of new anticorrosion coatings. This is caused by the limited overlap between the modelled conditions and the actual corrosion protection that is achievable by the anticorrosion system over a period of time.

In the present work the inhibitor diffusion through a coating towards a damage location is modelled using a multi physics finite elements method (FEM) using the design parameters for anticorrosion primers as variables. For simplification, a minimum local inhibitor concentration for corrosion protection is considered without taking the actual corrosion and deposition reactions at the metal-electrolyte interface into account due to their fast reaction speeds in comparison with the other rate-controlling steps in the process. The obtained parameters are used to calculate the transport of inhibiting species from the coating towards the electrolyte interface by mass conservation, assuming a homogeneous system with random dispersion of inhibitors (located initially in the discrete carriers) and charge neutrality of the solution. The results from the transport models are used to predict the maximum obtainable period of inhibition at damaged location under immersion conditions whereby the damage size, carrier size, PVC and interconnected pathways are taken as most important input parameters.

To validate the results from the model, a range of epoxy coatings with inhibitor content and damage dimensions comparable to the systems modelled were prepared and tested using a recently developed opto-electrochemical setup. Cerium is used as model inhibitor and stored following previously reported procedures using both nano-particles [26] and micro-particles [27,28]. Based on previous reports, the cerium concentration should preferably be between 10^{-5} and 10^{-3} M and not higher than 10^{-2} M [29–32]. In this work a minimum local concentration of 10^{-5} M after 100 s immersion will be considered as sufficient for protection to avoid any over-estimation on the simulated minimum required inhibitor release rate. The effect of damage diameter, carrier size, PVC and connecting inhibitor pathways on the degree of corrosion protection are studied for the case of epoxy-coated AA2024-T3, damaged and immersed in 0.05 M NaCl.

2. Computational and experimental details

2.1. Geometrical details

Fig. 1 illustrates the geometry of the coating system with the damage dimensions and the electrolyte volume it was exposed to. The same geometrical parameters and dimensions were used for the simulations and the validating corrosion experiments.

The electrolyte is shown in Fig. 1 (in blue) is composed by three interfaces: namely two cone-shaped volumes with an apex angle of 30° (S1, where the electrolyte is in contact with the primer, and S2, where the electrolyte is in contact with the topcoat) and a larger cylinder (S3) to establish the dimensions of the electrolyte on top of the coating system. The primer contains homogeneously distributed NaY zeolites or diatomaceous earth (DE) as either nano-, or micro-carriers at a defined pigment volume concentration (PVC) and inhibitor loading levels of the carriers (. The diameter of the damage at the metal surface (Ø) and the coating composition (i.e. pigment type, PVC and inhibitor loading) are varied in the simulations and experiments. In the simulations this exposed metal surface is considered to be inert (i.e. no local release or
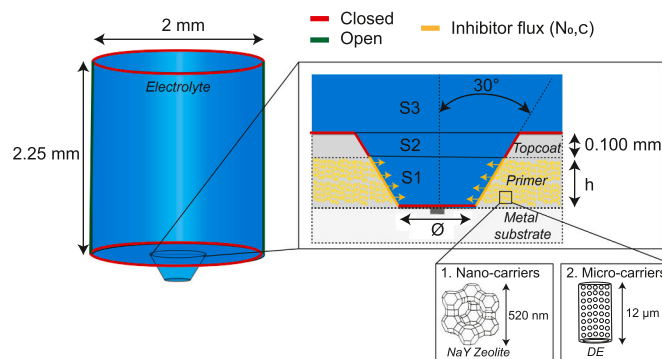

Fig. 1. Graphical illustration of the 3D model representing the anticorrosion coating with its damage (i.e. circular hole) and the electrolyte volume it is exposed too. A non-permeable topcoat is used to attain only for the lateral inhibitor release towards the damage. The inset shows the two carriers loaded with cerium salt used in this work.

uptake of the inhibitor species) and a minimum accumulated inhibitor concentration at the metal surface is considered as the governing condition for protection. The boundaries at the side walls of S1 represent the damaged coating primer surface (shown in orange in Fig. 1). From this boundary a flux of diluted inhibitor species is assumed (i.e. dissolved inhibitors moving from the coating boundary towards the centre of the electrolyte). S2 represents the electrolyte enclosed by the topcoat walls, S1 and S3. S2 has a fixed height of 100 µm with closed external boundaries (no release or uptake by the topcoat or from S1). S3 is the modelled electrolyte volume above the coating. In this case, the sides of the cylinder are open in order to simulate the exposure of the damage to a similar electrolyte field compared to the experimental conditions. The top of the modelled domain is the electrolyte surface located 2.25 mm above the metal surface.

2.2. Diffusion-limited model for inhibitor transport in the electrolyte

A 3D finite element model (FEM) is built in COMSOL Multiphysics® 5.4 (build: 225) to predict the concentration gradients of inhibitor species in the electrolyte (in S1, S2, and S3) as a result of the diffusional flux through the primer walls at the damage location (shown by orange arrows in Fig. 1). The FEM model calculates the required flux of inhibitors from one surface (electrolyte/inhibitor-containing-coating interface) towards another surface (electrolyte/metal interface). This FEM model thereby only simulates the effects that occur at the coating/electrolyte interface while coating parameters such as pigment volume concentration are considered in the kinematic model discussed in 2.3. The 3D CAD model of the electrolyte (Fig. 1) is built in CATA V5R20 and imported as a solid step file into COMSOL with an absolute tolerance of 1.0×10^{-5} mm. In these simulations the dissolution and diffusion of the inhibitor through the coating is considered to be instantaneous. Hence, the transport of diluted inhibitors in the electrolyte is modelled given the boundary conditions as explained in the previous section. The transport is assumed to be concentration-driven diffusion-limited; that is, convection and migration by an electric field in the electrolyte are not taken into account. The model also assumes that the inhibitor species are dilute ($<10^{-1}$ M) at the coating/electrolyte interface. These conditions are assumed to be realistic since only a limited amount of highly soluble inhibitors is already in a dissolved state when they cross the coating-electrolyte interface, allowing the inhibitor concentration to remain below the solubility limit. The density and viscosity of the electrolyte containing inhibitors can be considered the same (less than 5%) as those of the solvent (H_2O) as reported in literature [33]. Under these conditions the following mass flow Eq. (1) for dilute species can be used to describe the diffusion of inhibitor i in the electrolyte:

$$\frac{\partial c_i}{\partial t} + \nabla \cdot J_i = R_i \tag{1}$$

where is the concentration of the inhibitor species (mol/m³), the mass flux relative to the averaged velocity (mol/(m²s)), and the mass flow reaction rate expression for the species (mol/(m³s)).

In this case the mass flux is based on the diffusion of molecular species through Fick's law as shown in Eq. (2):

$$J_i = -D_c \nabla c_i \tag{2}$$

where D_c is the inhibitor diffusion coefficient (m²/s), which can be varied in the simulations.

The initial conditions of the model assume that there are no inhibitor species present at the start ($t = 0$; $C_{bulk} = 0$) and that there is a constant release flux ($N_{0,c}$ in mol/(m²s)) of a predefined number of inhibitor species (**n**) at the primer-coating boundary as shown in Fig. 1 and Eq. (3):

$$N_{0,c} = -\boldsymbol{n} \cdot J_i \tag{3}$$

For the simulations a standard mesh is used, consisting out of 7292 elements with an average quality of 0.66. The time-dependent calculations are executed with a step-size of 1 s on 7931 internal and 1501 external degrees of freedom within the mesh. The release-flux, inhibitor diffusion coefficient and damage size are varied during the different simulations to investigate their effect on the inhibitor concentration profiles at and near the damage location over a period of 10 ks after initial exposure. In this work it is assumed that the inhibitor release from the carriers and through the coating is fast enough to reach this inhibitor concentration.

2.3. Inhibitor depletion from carriers at the primer-electrolyte interface

The amount of released inhibitor from the carriers embedded inside the coating can be calculated using a kinematic model whereby the inhibitor release flux ($N_{0,c}$) from the diffusion-limited model for the electrolyte is coupled to a representative damage geometry and coating composition. The inhibitor mass flow reaction rate taking place at the coating-electrolyte interface over a period of time (t) can be obtained from the diffusion rate using the principle of mass conservation:

$$\frac{dR_i}{dt} = N_{o,c} = m_i \frac{\cos(30°)}{\boldsymbol{\pi}\varnothing ht} \tag{4}$$

where is the available inhibitor species (molar) that can be released from the coating interface.

As a first order approximation, the calculations on the coating are described in terms of homogeneously distributed inhibiting species from the carriers without taking transport properties (i.e. linearization) and electro-migration of the electrolyte into consideration. The coating-side of the interface is shown in more detail in Fig. 2 and schematically depicts the inhibitor release from the coating for two carrier/network configurations.

In the first configuration (Fig. 2a) it is assumed that the inhibitors are released from the particles or inhibitor clusters with size (P) located at a distance (L) from the coating-electrolyte interface, whereby $0 < L \leq P$. In the second configuration it is assumed that the inhibitors are also released from particles located inside the coating with inhibitor transport through an interconnected diffusive network (L > P). The inhibitor (molar) mass can be calculated as a portion of the total mass of the coating around the damage without taking the particle shape into account. For both configurations the following kinematic equation can be used, whereby the weight of available inhibitor species is calculated by taking the total coating volume around the damaged area at a variable distance (L), together with the total coating density (ρ_c) containing a pigment volume concentration of loaded particles (PVC) that contain a percentage of active inhibitor species (with molecular weight (Mw_i):

$$m_i = \frac{\left(\frac{\pi h \left(\frac{\varnothing}{2}+L\right)^2}{\cos(30°)} - \frac{\pi h \left(\frac{\varnothing}{2}\right)^2}{\cos(30°)}\right) PVC \cdot \rho_c \cdot \gamma_i}{Mw_i} \tag{5}$$

Considering Eqs. (4) and (5) the maximum release rate (N_{max}) that can be reached over a period of time (t) before the inhibitor population at a distance from the crack is completely depleted. This can be expressed using Eq. (6), whereby the penetration distance (L) is the only geometrical variable for a given coating composition and damage geometry:

$$N_{max} = \frac{\rho_c \cdot PVC \cdot \gamma_i}{Mw_i \cdot t \left(\frac{L^2}{\varnothing} + L\right)} \tag{6}$$

The model can also be used to describe the depletion time as the moment when the inhibitor species are completely depleted form their carriers in combination with the inhibitor release flux ($N_{0,c}$) from the diffusion-limited model in Eq. (7):

$$t_{depletion} = \frac{\rho_c \cdot PVC \cdot \gamma_i}{Mw_i \cdot N_{0,c} \left(\frac{L^2}{\varnothing} + L\right)} \tag{7}$$

2.4. Materials and samples preparation for experimental validation

2.4.1. Materials

NaY zeolites (CBV 100) with a SiO_2/Al_2O_3 mole ratio of 5.1 and a particle size of 520 ± 50 nm are purchased from Zeolyst International and used as-received. Diatomaceous earth (Diafil 525) is supplied by Profiltra Customized Solutions (NL). After cleaning the diatomaceous earth following a procedure reported elsewhere [27], a mixture of cylinder-shaped micro- to nano-porous amorphous silica particles with a mean particle size of 12 ± 5 μm is obtained. Cerium nitrate hexahydrate ($Ce(NO_3)_3 \cdot 6H_2O$) and dimethylformamide (DMF, ≥99.9%) are used in the inhibitor loading process. 2 mm thick bare copper-rich aluminium
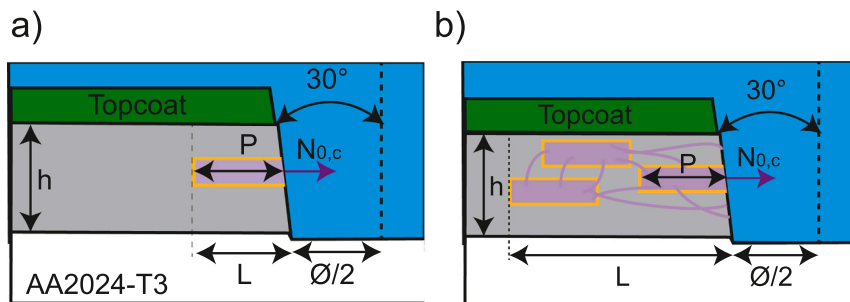

Fig. 2. Graphical illustration of the damaged coating to study inhibitor release for (a) single carriers directly exposed to the electrolyte interface and (b) interconnected network of particles.

alloy 2024-T3 (AA2024-T3) panels are supplied by Kaizer Aluminium and used as substrate. Commercially available bisphenol-A-based epoxy resin (Epikote™ 828 with 184–190 g/eq. epoxy) and amine crosslinker (Ancamine®2500 with 105–110 g/eq. H$^+$) are supplied by AkzoNobel (NL) and used as-received to form the coating binder. Xylene (99%) is used as solvent in the coating formulation. Milipore® Elix 3 UV filtered water is employed in all steps requiring water.

2.4.2. Loading nano- and micro-carriers with inhibitor

The cerium loading of the zeolite and diatomaceous earth is carried out following previously reported procedures through ion exchange [26] and local precipitation by controlled solvent evaporation [28], respectively. After loading, the effective release was measured with UV-VIS using previously reported procedures [26,28]. the resulting Ce-loaded zeolites (CeY) contain 12 ± 0.5 wt% Ce^{3+} cations in their structure (active inhibitor species), while the Ce-loaded diatomaceous earth (CeDE) contain 50 wt% $Ce(NO_3)_3 \cdot 6H_2O$, which is equivalent to 16 wt% Ce^{3+} cations.

2.4.3. Coatings formulation and application

Coupons of 200×250 mm are cut from the same 2 mm thick AA2024-T3 panel. The native oxide layer is removed using a 320 grit SiC paper for at least 5 min until the entire surface appears bright and containing fresh scratches. The panel is degreased with acetone and sonicated in ethanol at 60 °C for 30 min. After air drying, a pseudo-boehmite treatment is performed on the coupons to increase the amount of reactive hydroxyl groups on the surface by 10 s immersion in 2 M NaOH followed by a 30 s immersion in distilled water and drying with nitrogen. The coupons are then stored in a dry and clean environment prior to coating for a maximum of 15 min.

Four different coating compositions are prepared (namely, REF, CeY, CeDE1 and CeDE2), as listed in Table 1. The coating binder formulation, identical for all coatings, is prepared using the g/eq. provided by the resins manufacturer for a stoichiometric epoxy reaction. In the presence of xylene as solvent, the weight-ratio used is 2.70:1.57:1.06 (epoxy:amine:solvent). The binder formulation is mixed for 5 min using a high-speed mixer at 2400 rpm and then left to pre-cure at room temperature for 30 min. After adding the inhibitor-loaded carriers, the coating formulation is manually stirred for 5 min and then applied onto the metal coupons using a doctor blade with wet thicknesses of 10/50/100 μm depending on the coating layer to be deposited. After a flash-off period of 30 min the samples are cured at 60 °C for 24 h to achieve full crosslinking and solvent evaporation. Smaller samples of 25×25 mm were cut and the dry coating thicknesses were measured using an eddy current probe. Only samples with a total coating thickness variance of less than 20 μm were used. The thicknesses of the selected samples for this experiment are indicated in Table 1. The samples are stored in a desiccator and taken out to acclimatize 30 min before damaging and corrosion testing.

Table 1
Composition and layer thicknesses of the four coating systems tested.

Name	Single layer	Carrier type	Carrier loaded with inhibitor	Dry thickness		ρ_c	PVC[1]
			(phr)	(μm)		(g/cm^3)	(%)
REF	Primer	–	–	100 ± 20		1.20	–
CeY	Primer	CeY	142	45	145	0.90	30
	Topcoat	–	–	100	± 20	1.20	–
CeDE1	Primer	CeDE	32	45	145	1.12	10
	Topcoat	–	–	100	± 20	1.20	–
CeDE2	Primer 1	–	–	10	155	1.20	–
	Primer 2	CeDE	140	45	± 20	0.98	30
	Topcoat	–	–	100		1.20	–

1

2.4.4. Controlled damages on coated panels

A Roland EGX-350 engraver equipped with a conical cemented carbide tip is used to create well-controlled circular damages to the coated panels prior to immersion in electrolyte for the corrosion studies. The engraving process stopped immediately after the first contact with the metallic surface, as detected using an LED and a closed electric circuit between the tip and the substrate. The engraving proceeded in steps of 10 μm in the z-direction perpendicular to the sample surface until the electric circuit closed (i.e. LED is ON). Damages with two different dimensions are created depending on the tip used: (i) 50 μm diameter damage with an AC125-BAL-PRO-0.002 with a tip-angle of 30° and (ii) 300 μm diameter damage with a ZECA-2025BAL with a tip-angle of 30°.

2.5. Corrosion evaluation with an in-situ optical and electrochemical set-up

All tests were performed using a recently developed optical-electrochemical setup [28,30,34]. The experiments aim to observe the occurrence of either corrosion or inhibitor-induced corrosion protection as a function of exposure time, and were designed to validate the results from the simulations. All experiments were repeated at least two times for each coating/damage configuration, producing comparable stages of corrosion and inhibition.

The optical-electrochemical setup is placed on an optical table equipped with active isolators and a damping breadboard. The table is then covered with a Faraday cage to avoid interferences from external electrical sources. The working principle of the setup is identical to the one described in our previous works [28,30,34]. Main difference with past works is that in the present work a commercial cell for Raman-electrochemistry studies from redox.me® (See Fig. SI-1 of support information) is used. The cell has a volume of 4.5 ml, an aperture opposite to a 1 mm thick quartz glass window of 3.5 cm^2 (i.e. exposed area of the studied sample to the electrolyte) and an optical path of 2.25 mm (i.e. distance between the sample and the quartz window). The cell is placed vertically on top of a manual translation stage that allowed positioning the damage in the field of view of the camera. This design of the Raman-cell can be regarded as an evolution of the cells described in earlier works [28,30,34], as it has a shorter optical path required for high magnification recording and is easier in handling and focussing the sample relative to the camera. A high-magnification USB camera from Dino-Lite, model AM7515MT4A (415-470×) with a 5.0 megapixel CMOS sensor (2592×1944 pixels) and an 8-LED ring-light is placed parallel to the glass window to monitor and illuminate the exposed area. The camera is controlled with DinoCapture 2.0 and programmed to record with a time interval of 1 min, simultaneously with the electrochemical measurements.

Highly resolved optical information at a resolution of 3 pixels/μm is obtained through an automated image analysis procedure using ImageJ software. After a recursive repositioning procedure the exposed metal surface is isolated from the surrounding coating by cropping, resulting in two sets of images. The images of the exposed metal surface are analysed using the previously described analysis method to calculate the surface fraction having undergone optical changes over time (related to corrosion) [35].

Under open-circuit conditions the local time-frequency behaviour of the Electrochemical Potential Noise (EPN) provides information about the corrosion kinetics, and so, the nature of the underlying physical-electrochemical processes [36–38]. The EPN signals are studied with a Hilbert-Huang transform through Matlab from Mathworks® based on a publicly available procedure from Rilling et al. [39,40]. This was combined with the use of published EPN spectra of the AA2024-T3 corrosion and inhibition by cerium under immersion conditions in a similar electrolyte [41]. In the present work, the described approach is used to identify localised corrosion, inhibition or passivation regimes as a function of the immersion time, as these regimes show clear

electrochemical differences. Examples of the Hilbert-Huang identification procedure can be found in SI-2. In short, the regimes for localised corrosion are identified by signals with comparable features found during measurements on local corrosion for AA2024-T3. The regimes for inhibition are identified by activity at a higher frequency compared to local corrosion on AA2024-T3, and the regimes of passivation by the lack of electrochemical activity, resulting in a low-frequency drift. Furthermore, 'inhibition' refers to 'inhibitor effect in a dynamic process' while passivation refers to a 'time independent process'.

3. Results and discussion

Simulated and experimental results are obtained for damaged epoxy coatings containing cerium loaded carriers. The coatings are applied on AA2024-T3 and exposed to electrolyte containing 0.05 M NaCl.

3.1. Diffusion-limited inhibitor release simulations

The following section discusses the effect of several coating and damage properties on the minimum required inhibitor release from anti-corrosive coatings containing homogeneously dispersed inhibitor clusters in the primer. The results are obtained using the diffusion-limited model of the electrolyte in combination with mass-conservation laws for the damaged coating system as explained in the experimental section.

3.1.1. Damage size

In real applications the thickness of the primer and the diffusion rate of the pigment are fixed while the damage size can vary. In line with this, Fig. 3 shows the effect of the damage diameter (Ø) on the minimum required inhibitor release rate needed for protection after 100 s of exposure, considered critical for an efficient protection. Representative predictions of the release rates required to reach 10^{-5} M at the centre of the damage are shown on the left side of Fig. 3 for Ø = 50, 300 and 1000 μm for the circled locations in the graph. It should be noted that this initial analysis is independent on the storage strategy of the inhibitor in the coating (i.e. dispersed or in containers).

The results in Fig. 3 show that higher release rates are required to protect larger damages (i.e. to provide sufficient inhibitor concentration

all over the damage at 100 s exposure). This result is expected and in good agreement with modeling and experimental results, showing a decrease in protected area at the centre of a damage when the size increases [17,18]. The decrease in protection is mainly due to the larger diffusion path that the inhibitor needs to travel through the electrolyte at the damage. The larger path requires larger diffusion gradients from the coating walls towards the centre of the metal surface. The required release rate shows a quadratic growth with the damage diameter as diffusion gradients towards the bulk solution above the damage increase. The simulations show that a minimum release rate of 4.2×10^{-8} mol/(m²s) for Ø = 50 μm and of 9.3×10^{-8} mol/(m²s) for Ø = 300 μm are required to achieve a minimum local concentration of 10^{-5} M for the protection of AA2024-T3 at the damage within 100 s. It is important to note that the effect of pH dependency is not taken into account in this simulation, and will likely affect the release rates for smaller damages as suggested elsewhere [17,18].

3.1.2. Carrier-size and PVC for sustained protection

When the inhibitors are loaded in carriers instead of homogeneously dissolved in the coating, the model needs to take into account the inhibitor depletion kinetics from the particles. The inhibitor depletion for the particles located at the coating-electrolyte interface can be calculated using Eq. (6) based on the inhibitor release rate simulations and the mass conservation laws. For these calculations it is not only assumed that the required inhibitor release rate and local inhibitor concentration at the damage wall is achieved within 100 s, but also that this can be sustained for at least 1000 s immersion by inhibitor diffusion from the particles to the damage location. These conditions thereby simulate the release rate to initiate protection within 100 s and sustain this for a period of at least 1000 s. Fig. 4 shows the simulated maximum inhibitor release rates (N_{max}) that can be achieved during this period for a damaged coating whereby the carrier-size (P) and PVC are varied.

Fig. 4 shows the expected result in accordance to literature where a higher inhibitor release rate is achieved by either adding more loaded carriers inside the coating (i.e. increasing the PVC) [21], or by using carriers with a larger particle size [22]. More interesting, and not described elsewhere, is the relationship between PVC and particle size in Fig. 4, showing that an increase of the PVC above 30% does not result in a significantly higher release rate while using larger carriers does
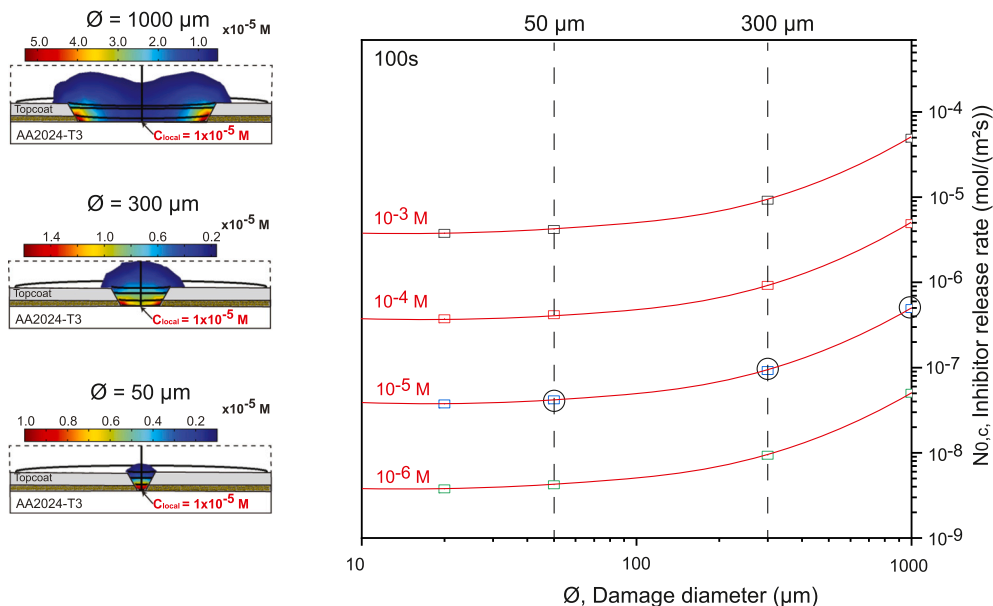

Fig. 3. Graph shows the effect of damage diameter (Ø) on the required inhibitor release rate (after 100 s of exposure. The red lines show the local inhibitor concentration at the centre of the damage. Schemes show the 2D cross-sections from the diffusion model at 10^{-5} M as indicated with circles. Model parameters: h = 45 μm, $D_c(Ce^{3+}) = 6.2 \times 10^{-10}$ m²/s.
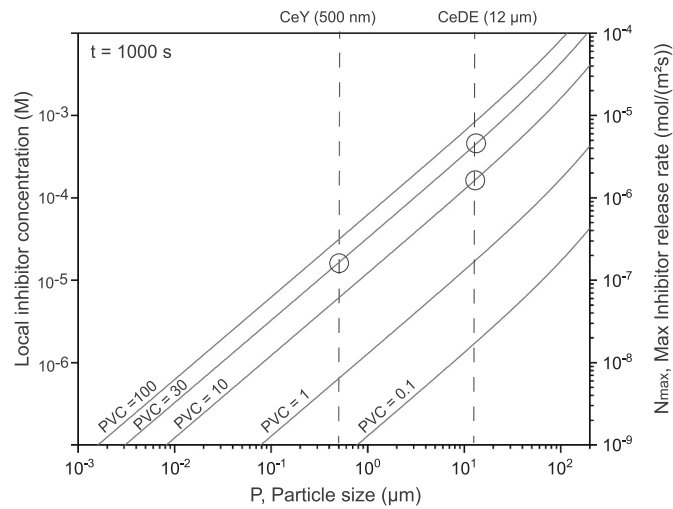
Fig. 4. Graph shows effect of particle size (P) and PVC on the maximum reachable inhibitor release rate (that can be maintained for 1000 s. Model parameters: Ø = 300 μm, =15% Ce^{3+} inside the carriers.

improve the behaviour, even at lower PVC. To validate the simulated results, the corrosion protection under immersion conditions is tested experimentally (and shown in 3.2) for damaged coatings containing: (i) 30 PVC nano-particles (CeY), (ii) 10 PVC micro-particles (CeDE1) and (iii) 30 PVC micro-particles (CeDE2).

3.1.3. Inhibitor pathways through the coating

In the previous section only the particles located at the coating-electrolyte interface are taken into account to study the maximum inhibitor release that can be sustained during 1000 s immersion. This scenario ultimately results in the depletion of inhibitor species from the nearest particles over longer immersion times (>1 ks). Fig. 5 shows the calculated time-dependent depletion (distance from the damage into the coating that shows inhibitor depletion at a given time). In this figure, the area below the black dotted line represents the Ce^{3+} depletion over time from a single-particle of 12 μm (e.g. DE particles). The area above the dotted line represents the depletion length into the coating over time considering that inhibitor pathways within the coating where created

and calculated using Eq. (7).

Fig. 5 shows that the release time, and therefore the amount of inhibitor being released over time, can be increased when interconnected paths between particles, i.e. networks, are created. Such connection paths enable the release and diffusion of Ce^{3+} ions located at relatively large distances from the damage. It should be noted that in this case, the inhibitor diffusion from particles further away from the damage edge has to take place before the particles at the coating-electrolyte interface are completely depleted in order to have a sufficient inhibiting power (i. e. sufficient corrosion inhibitor release).

The same calculations as shown in Fig. 5 are performed for all the coating and damage geometries validated experimentally at a later stage. Table 2 shows the inhibition period that can be achieved for these systems, assuming a minimally required inhibitor release rate from the coating to maintain a local concentration of 10^{-5} M at the centre of the damage. The inhibition period is calculated considering: (i) release achieved by single particles at the damage (L = P) and (ii) release achieved when an interconnected network exists with a penetration depth (L) of 50 μm from the damage wall.

The results in Table 2 show that the coatings with CeY nano particles are only able to protect for a relatively short period of time. For CeY coatings it is thereby critical to achieve interconnected pathways early on to keep the local inhibitor concentration at or above the minimum required limit of 10^{-5} M. The coatings containing CeDE1 particles show an inhibition period that is 5 to 10 times longer compared to the CeY

Table 2
Corrosion inhibition periods in case of (i) single particle release and (ii) in the presence of interconnected pathways obtained through simulation. The same conditions are later one tested experimentally.

Coating system	Damage diameter	Inhibition period maintaining $C_{local} = 1 \times 10^{-5}$ M	
		Single particle release	Interconnected pathways[a]
CeY	50 μm	1.7 ks	23 ks
	300 μm	1.2 ks	13 ks
CeDE1	50 μm	18 ks	120 ks
	300 μm	15 ks	70 ks
CeDE2	50 μm	47 ks	315 ks
	300 μm	39 ks	184 ks

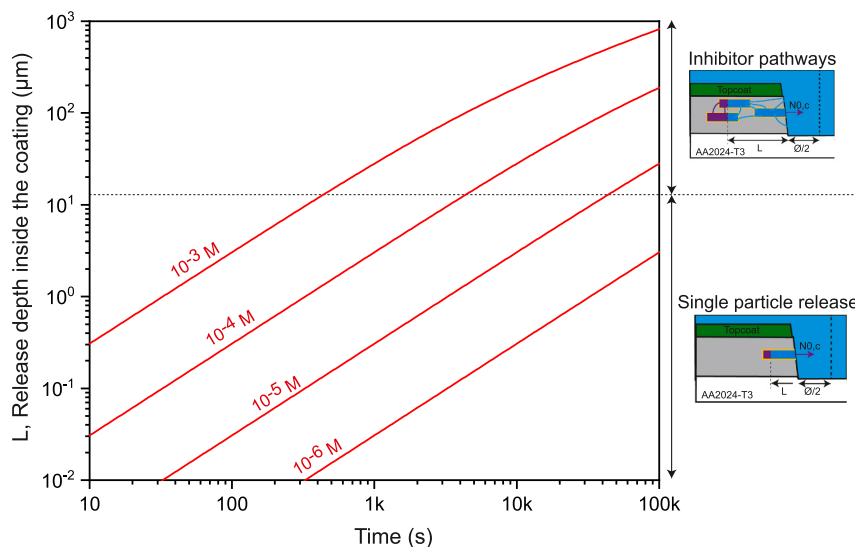[a] Maximum distance into the coating = 50 μm.

Fig. 5. Calculated time-dependent inhibitor release from CeDE particles located at the surface of the coating at the damage location (below dotted line) and the release resulting from the presence of an interconnected network of particles (above dotted line). Model parameters: Ø = 300 μm, =15% Ce^{3+} inside the carriers, PVC = 30, P = 12 μm.

coating. This is remarkable because the CeDE1 coating contains a lower amount of inhibitor species (10 PVC) compared to the CeY coating (30 PVC) thereby suggesting that larger particles are more efficient than smaller ones even at lower PVC. The CeDE2 coating contains the same PVC as the CeY coating, and shows the longest inhibition period. The calculations show that larger particles and higher PVC can significantly increase the initial period of protection when considering active particles are single particles in direct contact with the damage. In turn, this allows more time for the creation of interconnected pathways and therefore sustained protection. It is good to note that the results show a best-case scenario and that shorter inhibition periods are more likely to occur due to higher release rates and incomplete inhibitor depletion from the particles at the damage.

3.2. Validation through optical-electrochemical experiments

The following section discusses the optical and electrochemical results obtained from the corrosion experiments using coating, damage and exposure conditions similar to those used in the simulation (Section 3.1). In this way the experimental results are used to validate the model results and the generic guidelines for the design of anticorrosive coatings based on carrier systems. All the experiments were repeated at least two times, whereby comparable optical and electrochemical results were observed.

Fig. 6 shows the experimental results of epoxy coatings without inhibitors applied on AA2024-T3 and used as reference system (REF). The results show the coatings behaviour with damages of $\varnothing = 50$ μm (small damage) or $\varnothing = 300$ μm (large damage) exposed to 0.05 M NaCl aqueous solutions. Fig. 6 a-b show the raw EPN signals. The background colour in these plots (grey in this case) indicates the type of activity based on the

Hilbert-Huang spectra (HHS) analysis as described in the experimental procedure shown in SI-2. As seen in Figs. 7 to 9, this background colour varies between grey (corrosion), green (inhibition) and yellow (passivation). Fig. 6 c-d show the untreated original optical images under immersion. While 6(e-f) show the images result of the software analysis of the optical images related to local activity.

The EPN signal (Fig. 6 a-b) as well as the HHS analysis, can be regarded as typical for the corrosion of AA2024-T3 under these conditions [41]. Hence, the grey background colour used indicates a stable localised corrosion process throughout the whole immersion period. The optical results (Fig. 6 c-d) show that pits appear at the metal surface in combination with oxide formation around the edge of the damage (i.e. top-right corner for the small damage) and are in line with previous measurements. The processed images (Fig. 6 e-f) show that the activity is localised at the exposed metal and at the interface between the coating and the metal surface (seen with the colour scale). No activity is observed at or underneath the coating itself (i.e. no delamination). The results show that the corrosion processes can be observed with high spatial and temporal precision using this optical-electrochemical approach.

3.2.1. The effect of damage size

Fig. 7 shows the optical and electrochemical results of epoxy coatings containing cerium-loaded nano-particles (CeY coating) in the presence of small ($\varnothing = 50$ μm) and large damages ($\varnothing = 300$ μm) and exposed to 0.05 M NaCl acqueous solution.

Fig. 7a shows initial inhibition (shown in green), followed by a period of limited corrosion activity around 2 ks (shown in grey) with a subsequent inhibiting period for the rest of the experiment. The optical images (Fig. 7c) and processed images (Fig. 7e) indicate that the exposed
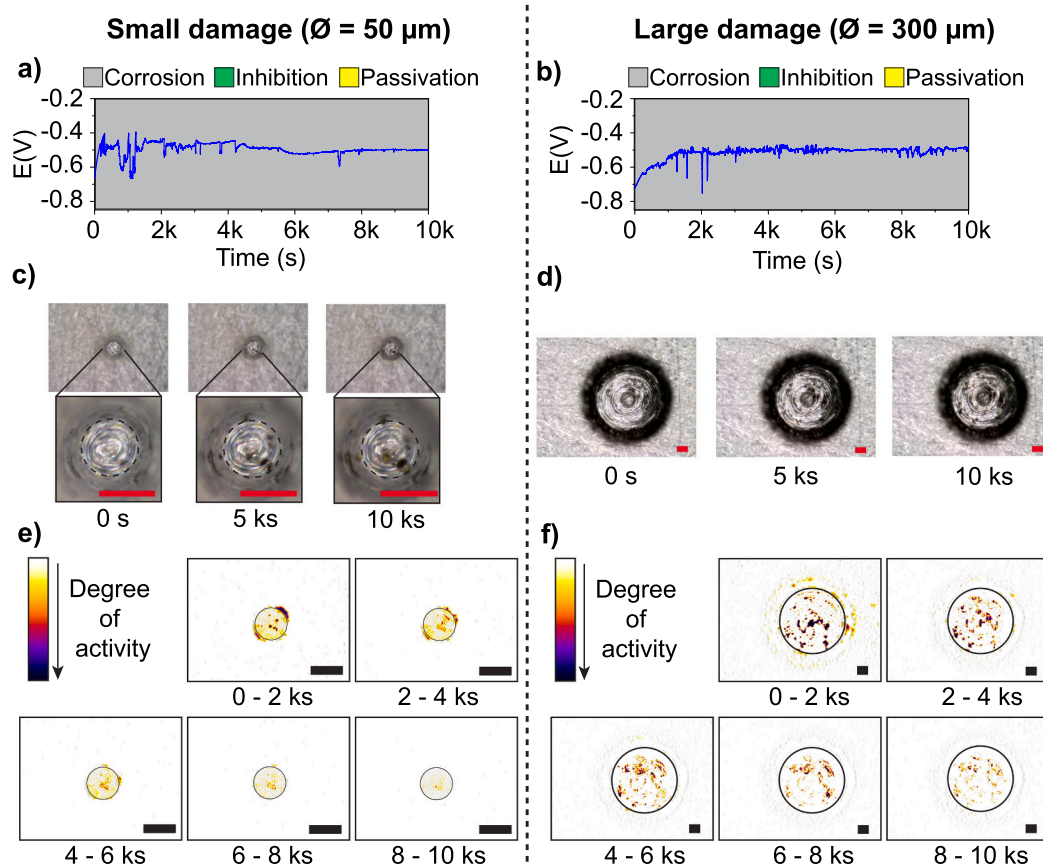

Fig. 6. Optical and electrochemical results for epoxy coatings during immersion in 0.05 M NaCl over a period of 10 ks containing a small damage (left) and a large damage (right). (a-b) are the raw EPN signals, (c-d) are the original images with a black dotted line located at the edge of the metal/coating interface, and (e-f) the software-calculated local activity maps. Scale bar represents 50 μm.
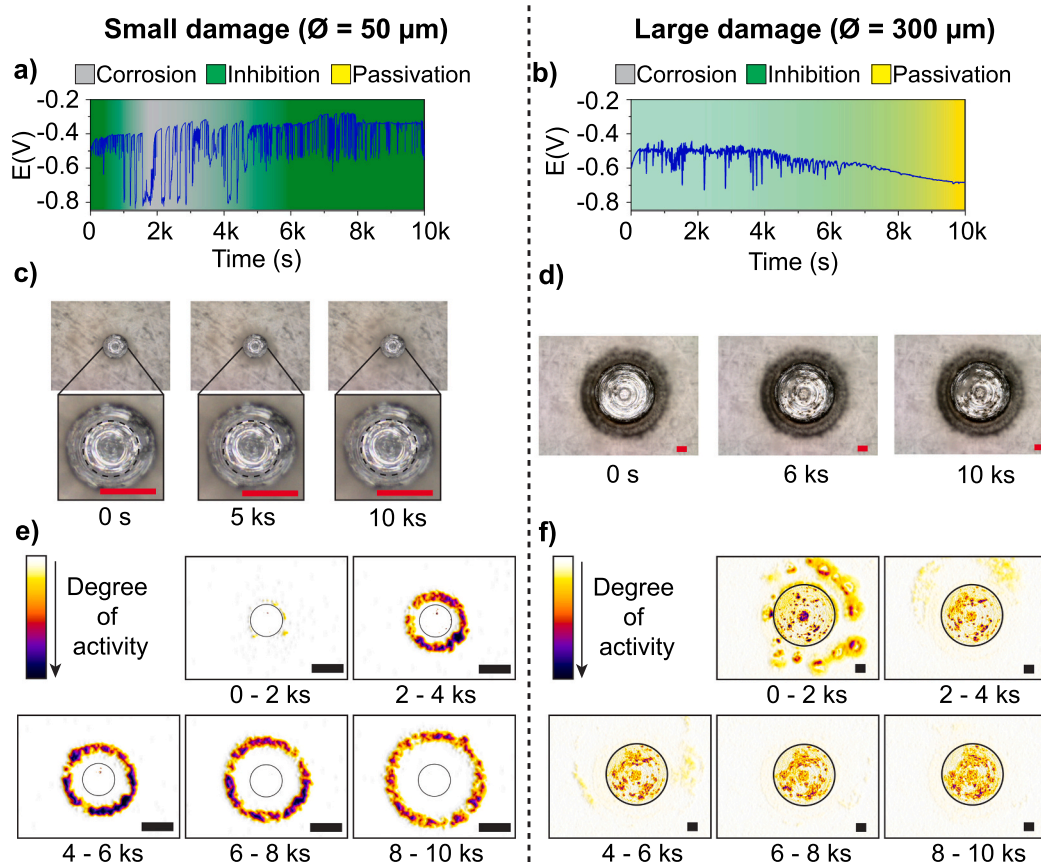
Fig. 7. Optical and electrochemical results for CeY coatings during immersion in 0.05 M NaCl over a period of 10 ks containing a small damage (left) and a large damage (right). (a-b) are the raw EPN signals, (c-d) are the original images with a black dotted line located at the edge of the metal/coating interface, and (e-f) the software-calculated local activity maps. Scale bar represents 50 μm.

metal (inside the black circle) does not show any sign of corrosion besides an isolated event between 2 and 4 ks that coincides with the 'corrosion' period identified in the EPN analysis. The simulation results (Table 2) for this damage size confirms that the inhibitor release rate for this coating composition is sufficiently high to prevent corrosion during the first 100 s. Another remarkable result is observed in the activity micrographs (Fig. 7e) which reveal a ring of high activity in the coating surrounding the exposed metal (i.e. the damage). This outside ring moves away from the damage centre with the immersion time, especially after 2 ks. The optical activity at the coating is likely to be the result of a change in the refractive index of the coating as observed in previous works [42]. This can be caused by one or a combination of different processes such as water ingress, inhibitor release, delamination and/or the formation of corrosion products underneath the coating. Unfortunately, the image analysis is yet unable to discern which of these is predominant but it confirms the expected behaviour in an inhibiting coating with water ingress from the damage site.

When the large damage is investigated, the EPN signal (Fig. 7b) and HHS analysis shows limited corrosion activity alternated with inhibiting events (shown in grey/green), followed by passivation (shown in yellow). The optical images (Fig. 7d) show that pits and oxides have formed inside the damage while the processed images (Fig. 7f) show that the activity at the metal is localised yet present in all the exposed area and occurs at high intensity (purple and red spots with sizes between 1 and 20 μm in radius). These results show that this anticorrosion coating is not effectively protecting the exposed metal surface due to an insufficient action of the corrosion inhibitor already from the early stages of immersion.

The optical-electrochemical results are in very good agreement with the diffusion-limited release simulation model (Fig. 3). The

experimental results confirm that a coating with inhibitor-loaded nanoparticles (e.g. CeY) that is very effective in the protection of relatively small damages (Ø = 50 μm), may be insufficient to protect large damages (Ø = 300 μm) already after 100 s. This is due to an insufficient inhibitor release rate as indicated by the model and suggests together with the simulation results, the need for higher PVC, discrete loading (i. e. larger particles) and/or inhibitor networks as will be analysed in the following sections.

3.2.2. The effect of particle size and PVC

Fig. 8 shows the processed optical-electrochemical results for CeDE1 and CeDE2 coatings containing a large damage (Ø = 300 μm) during immersion in 0.05 M NaCl. In addition, the CeDE2 coating contains a thin 10 ± 5 μm pure epoxy layer between the metal and the inhibitor-loaded epoxy. The thin epoxy-amine coating layer between the metal surface and the epoxy layer loaded with inhibitor prevented, during the studied immersion conditions, the presence of corrosion processes at undamaged locations through barrier increase. In this case all the optical activity observed outside the damage can only be related to electrolyte and/or inhibitor transport inside the inhibitor-containing layer. The EPN signal and HHS analysis for both coatings (Fig. 8 a-b) shows inhibition activity (shown in green), with limited corrosion at the end of the exposure for the case of 10 PVC (shown in grey). The optical images (Fig. 8 c-d) and the processed images (Fig. 8 e-f) for both coatings confirm the lack of corrosion activity. This indicates a clear protection against corrosion without significant water ingress in the coating (absence of the activity ring at the coating around the damage as observed in Fig. 7).

When comparing the CeY coating shown in Fig. 7 (i.e. PVC = 30) with the CeDE2 (same PVC and inhibitor loading but larger carriers), the
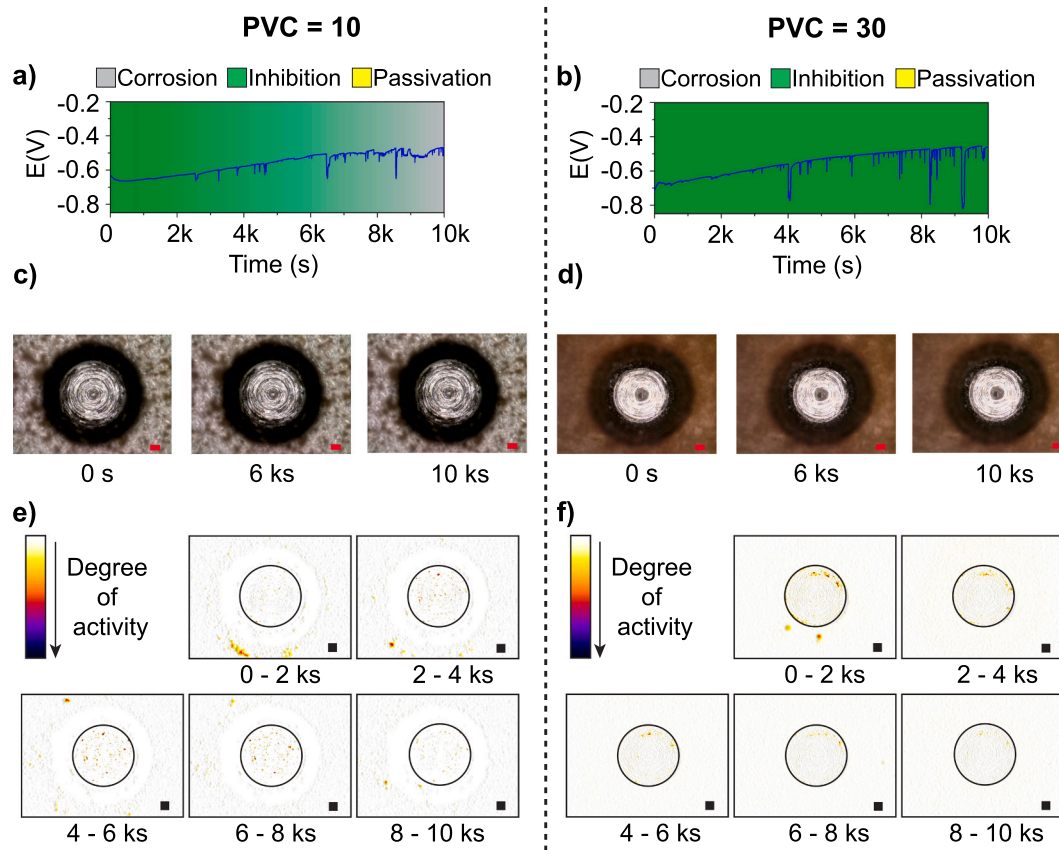
Fig. 8. Optical and electrochemical results for CeDE coatings during immersion in 0.05 M NaCl over a period of 10 ks containing 10 PVC (left) and 30 PVC (right) micro-carriers. (a-b) are the raw EPN signals, (c-d) are the original images and (e-f) the software-calculated local activity maps. Scale bar represents 50 μm.

results clearly suggest the benefit of using larger particles as was predicted in the simulations: CeDE2 shows clear effective corrosion protection while CeY nanoparticles are insufficient to protect large damages. Nevertheless, since the zeolite system relies on ion exchange of Ce^{3+} and the DE relies on dissolution of $Ce(NO_3)_3$ for the release of the inhibitor, it is not possible to discard the influence of the binding type between the carrier and the inhibitor on the effective corrosion protection, even though this distinction is not considered in the simulation experiments while similar results are obtained. Furthermore, selection of the carriers-inhibitor will not affect the results because the concept relies on sufficient amounts of inhibitor release on site. Size and/or binding type exert such a large influence on the inhibition that coatings with significantly lower PVC (CeDE1) still show significantly higher levels of protection than the coating with 30 PVC nanocarriers. These results are in any case in good agreement with the model (Fig. 4), which predicted that a higher release rate can be achieved with larger particles. Similar results are obtained for the CeDE coating containing a small damage (Ø = 50 μm), shown in SI-3.

3.2.3. The effect of inhibitor pathways

The experimental results in Fig. 8 show that both 10 and 30 PVC CeDE particles provide sufficient protection for a short period of time. Also the simulation results shown in Table 2 suggest that for this time-period (< 15–18 ks) the release of inhibitors from particles located at the particle-electrolyte interface would be sufficient to yield protection. Nevertheless, to reach an extended protection time the model suggests that the creation of inhibitor pathways would be desirable. The diffusion within the coating can be promoted by increasing the PVC (i.e. shorter particle-particle distance). In this section the effect of diffusion pathways on the corrosion protection is investigated for the CeDE coatings containing 10 and 30 PVC at relatively long immersion times (50 ks) for

small and large damages. Fig. 9 shows the optical results for a small damage (left side) and a large damage (right side) during immersion in 0.05 M NaCl.

The EPN signal and HHS analysis for the small damage in 10 PVC (Fig. 9a) starts with inhibiting activity (shown in green). Subsequently, from 8 to 20 ks, some limited localised corrosion is detected (shown in grey). At immersion times >20 ks a passive state is detected (shown in yellow), which is in good agreement with the simulated protection time of 18 ks when no interconnected pathways exist, as shown in Table 2. When the damage is larger (Fig. 9b), the same coating of 10 PVC shows inhibiting activity only during the first 7.3 ks. After this initial inhibition, corrosion gradually becomes more dominant with very characteristic transients for AA2024-T3 in a NaCl solution. Additionally, this result is in good agreement with the predicted protection time of 15 ks for the single-particle release at the damage/electrolyte interface. The optical images and analysis for 10 PVC (Fig. 9 c-d) suggest surface activity at long immersion times. This is more evident when the treated images are observed (Fig. 9 e-f). The small damage (Fig. 9 c and e) shows some darkening of the exposed metal surface in combination with several black spots (localised corrosion) and very high activity in the analysed colour plot. Similar darkening of the entire surface is observed in control samples in which the REF coating system was damaged, after which these were immersed in 0.05 M NaCl containing 10^{-6} M cerium nitrate, which is below the minimum required for corrosion protection (SI-4). This control test suggests that 10 PVC is unable to release sufficient Ce^{3+} over longer immersion times (>10 ks). Additionally, the large damage (Fig. 9 d and f) shows local activity (i.e. pits and co-operative corrosion) and high local activity at the metal surface similar to the REF coating, however to a lesser extent and appearing after longer immersion-times.

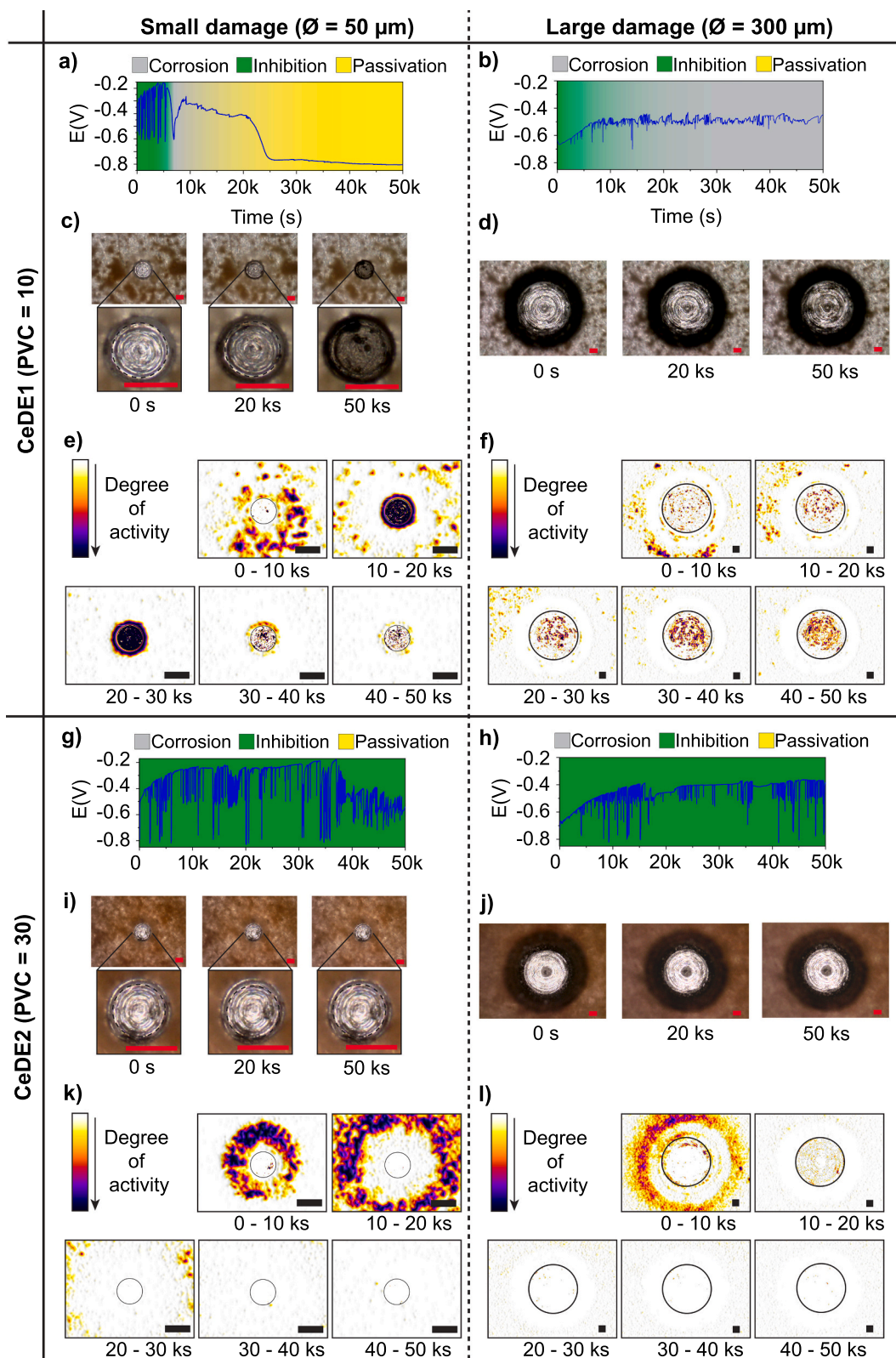In the case of 30 PVC, where inhibiting paths are expected, the EPN

Fig. 9. Optical and electrochemical results for coatings containing CeDE particles at 10 PVC and 30 PVC during immersion in 0.05 M NaCl over a period of 50 ks. Coatings contain a small damage (left) and a large damage (right). Scale bar represents 50 μm.

signals from the small as well as the large damage (Fig. 9 g-h) show variable transient densities and amplitudes. The HHS analysis indicates that these transients are associated with inhibitor activity in both cases. The optical images for 30 PVC (Fig. 9 i-j) show the total absence of signs related to corrosion over the period of 50 ks in both cases. These results

are a clear indication that higher PVCs result in a longer protection period, in particular when there is a network of interconnected particles, as shown in Table 2. The local activity maps (Fig. 9 k-l) show a significant amount of activity at the coating near the damage (ring) moving away from the damage centre during the first 20 ks and 10 ks for the

small and large damage, respectively. This similar process was observed for the CeY coating containing a similar PVC (Fig. 7), yet at much shorter times (<10 ks) and is not present in the case of coatings without inhibitors or at lower PVC. This, together with the high degree of protection observed, supports the idea that the optical changes of the coating (ring) are related to the electrolyte diffusion in the coating due to the particle interconnections induced by a sufficiently high PVC. Although not analysed in this work, the speed of the movement of the ring outside the damage centre may be related to the electrolyte ingress kinetics. The electrolyte path observed with the activity rings may confirm the long-time protection through gradual dissolution of Ce^{3+} from locations outside the damage and its diffusion towards the damage location. These results confirm the predictions obtained with the simplified simulation model (Fig. 5 and Table 2) which indicate that there will be a rapid transition to incomplete protection when no pathways are present. These results support the underlying idea from previous experimental works that the creation of inhibitor diffusion pathways within the coating is of utmost relevance to facilitate efficient corrosion protection for long immersion times.

4. Conclusions

In this work, a simplified diffusion-driven inhibitor transport model based on kinematic mass-conservation laws is introduced as a first order approximation tool to determine the required design parameters for anticorrosive coatings containing carriers loaded with inhibitors. The model is used to calculate the minimum required inhibitor concentration at the metal surface for protection. The simulations are validated with experiments performed on epoxy coatings containing either zeolites as nanocarriers or diatomaceous earth as microcarriers, loaded with cerium salt as inhibitor. The simulated results show that quadratic growth of release rates is required to achieve protection of larger damages over long immersion times. Simulation and experimental results indicate that nano-particles loaded with corrosion inhibitors are only able to protect small damages in the low-micron range even at high PVC contents. For comparably high PVC or lower PVC, both simulations and experiments suggest that larger carriers (in the range of several micron) result in significantly higher inhibitor release rates and a tenfold longer protection times, even at lower inhibitor content inside the coating. The simulations predict that even longer protection times may be possible when interconnected inhibitor diffusion pathways inside the coating are created. This is validated experimentally using a combined optical and electrochemical method. Maps of local activity obtained from optical analysis under immersion show the presence of activity rings around the damage not visible in unloaded coatings. These activity rings around damages, are attributed to the diffusion of electrolyte and inhibitors from the damage site into the coating and are related to the achieved sustained inhibitor release and long-term protection at a damage sites. This highlights the need of more fundamental research on how these interconnected pathways can be created, whereby more extensive diffusion models will be required to investigate the release rate trough porous coating/carrier/inhibitor interfaces.

CRediT authorship contribution statement

Paul J. Denissen: Conceptualization, Investigation, Methodology, Formal analysis, Writing – original draft, Writing – review & editing, Visualization. **Axel M. Homborg:** Methodology, Formal analysis, Writing – review & editing. **Santiago J. Garcia:** Conceptualization, Methodology, Writing – original draft, Writing – review & editing, Visualization, Supervision.

Declaration of competing interest

The authors declare that they have no known competing financial interests or personal relationships that could have appeared to influence the work reported in this paper.

Appendix A. Supplementary data

Supplementary data to this article can be found online at https://doi.org/10.1016/j.surfcoat.2021.127966.

References

[1] J.E.O. Mayne, The mechanism of the protective action of an unpigmented film of polystyrene, J. Oil Colour Chem.Assoc. 32 (1949) 481–487.

[2] A.A. Roche, J. Guillemenet, Mechanical and chemical properties of organic coatings applied to metallic sheet substrates, Thin Solid Films 342 (1999) 52–60, https://doi.org/10.1016/S0040-6090(98)01340-6.

[3] J.E.O. Mayne, How paints prevent corrosion, Anti-Corrosion Methods Mater. 1 (1954) 286–290, https://doi.org/10.1108/eb018973.

[4] W. Funke, H. Haagen, Empirical or scientific approach to evaluate the corrosion protective performance of organic coatings, Ind. Eng. Chem. Prod. Res. Dev. 17 (1978) 50–53, https://doi.org/10.1021/i360065a014.

[5] X.F. Yang, C. Vang, D.E. Tallman, G.P. Bierwagen, S.G. Croll, S. Rohlik, Weathering degradation of a polyurethane coating, Polym. Degrad. Stab. 74 (2001) 341–351, https://doi.org/10.1016/S0141-3910(01)00166-5.

[6] F. Deflorian, S. Rossi, L. Fedrizzi, C. Zanella, Comparison of organic coating accelerated tests and natural weathering considering meteorological data, Prog. Org. Coat. 59 (2007) 244–250, https://doi.org/10.1016/j.porgcoat.2006.09.036.

[7] F.X. Perrin, C. Merlatti, E. Aragon, A. Margaillan, Degradation study of polymer coating: improvement in coating weatherability testing and coating failure prediction, Prog. Org. Coat. 64 (2009) 466–473, https://doi.org/10.1016/j.porgcoat.2008.08.015.

[8] S.B. Lyon, R. Bingham, D.J. Mills, Advances in corrosion protection by organic coatings: what we know and what we would like to know, Prog. Org. Coat. 102 (2017) 2–7, https://doi.org/10.1016/j.porgcoat.2016.04.030.

[9] A.E. Hughes, I.S. Cole, T.H. Muster, R.J. Varley, Designing green, self-healing coatings for metal protection, NPG Asia Mater. 2 (2010) 143–151, https://doi.org/10.1038/asiamat.2010.136.

[10] A.E. Hughes, A. Trinchi, F.F. Chen, Y.S. Yang, I.S. Cole, S. Sellaiyan, J. Carr, P. D. Lee, G.E. Thompson, T.Q. Xiao, The application of multiscale quasi 4D CT to the study of SrCrO4 distributions and the development of porous networks in epoxy-based primer coatings, Prog. Org. Coat. 77 (2014) 1946–1956, https://doi.org/10.1016/j.porgcoat.2014.07.001.

[11] A.E. Hughes, A. Trinchi, F.F. Chen, Y.S. Yang, I.S. Cole, S. Sellaiyan, J. Carr, P. D. Lee, G.E. Thompson, T.Q. Xiao, Revelation of intertwining organic and inorganic fractal structures in polymer coatings, Adv. Mater. (2014), https://doi.org/10.1002/adma.201400561.

[12] S.G.R. Emad, X. Zhou, S. Morsch, S.B. Lyon, Y. Liu, D. Graham, S.R. Gibbon, How pigment volume concentration (PVC) and particle connectivity affect leaching of corrosion inhibitive species from coatings, Prog. Org. Coat. 134 (2019) 360–372, https://doi.org/10.1016/j.porgcoat.2019.05.008.

[13] M.T. Rodríguez, S.J. García, J.J. Gracena, K.A. Habib, J.J. Suay, Influencia de la concentración de pigmento en volumen (CPV) en las propiedades de una imprimación epoxi, Rev. Metal. 41 (2005) 202–207, https://doi.org/10.3989/revmetalm.2005.v41.iextra.1025.

[14] M.T. Rodríguez, J.J. Gracena, J.J. Saura, J.J. Suay, The influence of the critical pigment volume concentration (CPVC) on the properties of an epoxy coating: part II. Anticorrosion and economic properties, Prog. Org. Coat. 50 (2004) 68–74, https://doi.org/10.1016/j.porgcoat.2003.10.014.

[15] A. Kalendová, D. Veselý, I. Sapurina, J. Stejskal, Anticorrosion efficiency of organic coatings depending on the pigment volume concentration of polyaniline phosphate, Prog. Org. Coat. 63 (2008) 228–237, https://doi.org/10.1016/j.porgcoat.2008.06.005.

[16] T. Prosek, D. Thierry, A model for the release of chromate from organic coatings, Prog. Org. Coat. 49 (2004) 209–217, https://doi.org/10.1016/j.porgcoat.2003.09.012.

[17] H. Wang, F. Presuel, R.G. Kelly, Computational modeling of inhibitor release and transport from multifunctional organic coatings, Electrochim. Acta 49 (2004) 239–255, https://doi.org/10.1016/j.electacta.2003.08.006.

[18] F.J. Presuel-Moreno, H. Wang, M.A. Jakab, R.G. Kelly, J.R. Scully, Computational modeling of active corrosion inhibitor release from an Al-co-ce metallic coating, J. Electrochem. Soc. 153 (2006) B486–B498, https://doi.org/10.1149/1.2335946.

[19] F. Thébault, B. Vuillemin, R. Oltra, K. Ogle, C. Allely, Investigation of self-healing mechanism on galvanized steels cut edges by coupling SVET and numerical modeling, Electrochim. Acta 53 (2008) 5226–5234, https://doi.org/10.1016/j.electacta.2008.02.066.

[20] R. Oltra, F. Peltier, Influence of mass transport on the competition between corrosion and passivation by inhibitor release after coating breakdown, Prog. Org. Coat. 92 (2016) 44–53, https://doi.org/10.1016/j.porgcoat.2015.11.024.

[21] E. Javierre, S.J. Garcia, J.M.C. Mol, F.J. Vermolen, C. Vuik, S. van der Zwaag, Tailoring the release of encapsulated corrosion inhibitors from damaged coatings: controlled release kinetics by overlapping diffusion fronts, Prog. Org. Coat. 75 (2012) 20–27, https://doi.org/10.1016/J.Porgcoat.2012.03.002.

[22] E. Javierre, Modeling self-healing mechanisms in coatings: approaches and perspectives, Coatings. 9 (2019), https://doi.org/10.3390/COATINGS9020122.

[23] J.R. Scully, N. Tailleart, F. Presuel-Moreno, Tunable Multifunctional Corrosion-resistant Metallic Coatings Containing Rare Earth Elements, Woodhead Publishing Limited, 2014, https://doi.org/10.1533/9780857093585.267.

[24] S.A. Furman, F.H. Scholes, A.E. Hughes, D. Lau, Chromate leaching from inhibited primers. Part II: modelling of leaching, Prog. Org. Coat. 56 (2006) 33–38, https://doi.org/10.1016/j.porgcoat.2006.01.016.

[25] A. Nazarov, D. Thierry, T. Prosek, N. Le Bozec, Protective action of vanadate at defected areas of organic coatings on zinc, J. Electrochem. Soc. 152 (2005) B220–B227, https://doi.org/10.1149/1.1924067.

[26] M. Abdolah Zadeh, J. Tedim, M. Zheludkevich, S. van der Zwaag, S.J. Garcia, Synergetic active corrosion protection of AA2024-T3 by 2D- anionic and 3D-cationic nanocontainers loaded with Ce and mercaptobenzothiazole, Corros. Sci. 135 (2018) 35–45, https://doi.org/10.1016/j.corsci.2018.02.018.

[27] P.J. Denissen, S.J. Garcia, Cerium-loaded algae exoskeletons for active corrosion protection of coated AA2024-T3, Corros. Sci. 128 (2017) 164–175, https://doi.org/10.1016/j.corsci.2017.09.019.

[28] P.J. Denissen, V. Shkirskiy, P. Volovitch, S.J. Garcia, Corrosion inhibition at scribed locations in coated AA2024-T3 by cerium- and DMTD-loaded natural silica microparticles under continuous immersion and Wet/Dry cyclic exposure, ACS Appl. Mater. Interfaces 12 (2020) 23417–23431, https://doi.org/10.1021/acsami.0c03368.

[29] M.A. Jakab, F. Presuel-Moreno, J.R. Scully, Critical concentrations associated with cobalt, cerium, and molybdenum inhibition of AA2024-T3 corrosion: delivery from Al-co-Ce(-Mo) alloys, Corrosion 61 (2005) 246–263, https://doi.org/10.5006/1.3280634.

[30] P.J. Denissen, S.J. Garcia, Reducing subjectivity in EIS interpretation of corrosion and corrosion inhibition processes by in-situ optical analysis, Electrochim. Acta 293 (2019) 514–524, https://doi.org/10.1016/j.electacta.2018.10.018.

[31] E.A. Matter, S. Kozhukharov, M. MacHkova, V. Kozhukharov, Electrochemical studies on the corrosion inhibition of AA2024 aluminium alloy by rare earth

[32] T.H. Muster, A.E. Hughes, S.A. Furman, T. Harvey, N. Sherman, S. Hardin, P. Corrigan, D. Lau, F.H. Scholes, P.A. White, M. Glenn, J. Mardel, S.J. Garcia, J.M.C. Mol, A rapid screening multi-electrode method for the evaluation of corrosion inhibitors, Electrochim. Acta 54 (2009) 3402–3411, https://doi.org/10.1016/j.electacta.2008.12.051.

[33] Chemical Reaction Engineering Module User's Guide, 1998. www.comsol.com/blogs. (Accessed 24 March 2020).

[34] P.J. Denissen, A.M. Homborg, S.J. Garcia, Interpreting electrochemical noise and monitoring local corrosion by means of highly resolved spatiotemporal real-time optics, J. Electrochem. Soc. 166 (2019) C3275–C3283, https://doi.org/10.1149/2.0341911jes.

[35] P.J. Denissen, In-situ Visual Quantification of Corrosion and Corrosion Protection, 2020, https://doi.org/10.4233/UUID:64F8F06E-5CC6-40CD-8C8D-722DA6304B06.

[36] A.M. Homborg, E.P.M. van Westing, T. Tinga, X. Zhang, P.J. Oonincx, G.M. Ferrari, J.H.W. de Wit, J.M.C. Mol, Novel time-frequency characterization of electrochemical noise data in corrosion studies using hilbert spectra, Corros. Sci. 66 (2013) 97–110, https://doi.org/10.1016/j.corsci.2012.09.007.

[37] S.J. García, H.R. Fischer, S. Van Der Zwaag, A critical appraisal of the potential of self healing polymeric coatings, Prog. Org. Coat. 72 (2011) 211–221, https://doi.org/10.1016/j.porgcoat.2011.06.016.

[38] A. Aballe, M. Bethencourt, F.J. Botana, M. Marcos, Wavelet transform-based analysis for electrochemical noise, Electrochem. Commun. 1 (1999) 266–270, https://doi.org/10.1016/S1388-2481(99)00053-3.

[39] P. Flandrin, G. Rilling, P. Gonçalvés, Empirical mode decomposition as a filter bank, IEEE Signal Process. Lett. 11 (2004) 112–114, https://doi.org/10.1109/LSP.2003.821662.

[40] G. Rilling P. Flandrin P. Gonçalvès , On Empirical Mode Decomposition and Its Algorithms, n.d.

[41] A.M. Homborg, E.P.M. Van Westing, T. Tinga, G.M. Ferrari, X. Zhang, J.H.W. De Wit, J.M.C. Mol, Application of transient analysis using hilbert spectra of electrochemical noise to the identification of corrosion inhibition, Electrochim. Acta 116 (2014) 355–365, https://doi.org/10.1016/j.electacta.2013.11.084.

[42] C.D. Dieleman, P.J. Denissen, S.J. Garcia, Long-term active corrosion protection of damaged coated-AA2024-T3 by embedded electrospun inhibiting nanonetworks, Adv. Mater. Interfaces 5 (2018), https://doi.org/10.1002/admi.201800176.